

**MSEC2020-8302**

## **NUMERICAL MODELING OF POWDER GAS INTERACTION FOR LASER POWDER BED FUSION PROCESS**

**Xuxiao Li, Wenda Tan<sup>1</sup>**

Department of Mechanical Engineering  
University of Utah  
Salt Lake City, UT

### **ABSTRACT**

*The powder motion induced by the gas flow has been identified as one of the critical phenomena in laser powder bed fusion processes that significantly affects the build quality. However, the gas dynamics and its induced driving forces for the powder motions have not been well quantified. A numerical model is developed to investigate such powder-gas interactions. With a combination of computational fluid dynamics and particle tracking techniques, the model is capable of simulating the transient gas flow field surrounding the powder and the forces exerted on powder surfaces. The interaction between metal powders and a free jet is investigated with the current model. In the simulation results, the entrainment and the ejection motions of powders with respect to the free jet can be predicted. It is found that the driving forces of these motions are majorly contributed by the pressure differences in the gas flow surrounding the powder, and the powders can also interact with the jet to significantly alter the flow field. Quantities which are difficult to measure by experiments are quantified by the simulations, such as the velocity and pressure field in the gas, as well as the subjected forces and torques of powders. Such quantitative information provides insights to the mechanisms of the powder-gas interaction in laser powder bed fusion processes.*

Keywords: Laser powder bed fusion, powder motion, multi-physics modeling

### **1. INTRODUCTION**

In the laser powder bed fusion (LPBF) process, a laser is directed towards and scans across a pre-deposited powder bed typically made of metal alloys. The metal powders are melted upon by the laser heating to form a molten pool, and are consolidated to attribute to the built part when the laser is moved away. The building process then repeats in a layer-by-layer manner to create the desired bulk geometries. It has recently been

revealed by optical high-speed imaging [1-3] and X-ray radiography [4-6] that, the powders tend to dislocate from its original location during the laser scanning. Specifically, the powders at a distance can be entrained towards the laser-shined region, while the powders nearby can be ejected from the laser-shined region.

It has been reported that the powder motions have significant influence to the build quality of LPBF. The ejected powders, when landing back on the build surface, can deteriorate the surface roughness [7], distort the molten pool geometry [8], or cause insufficient melting and lack-of-fusion defects [4]. Moreover, the apparent stochastic nature of these powder motions [1] randomizes of the mass distribution of the powder bed and increases the uncertainty of the build quality.

In literature, the origin of the powder motions has been explained based on experimental observations and basic principles of physics [3, 4]. The intense laser heating of the metal powders triggers metal vaporization. A metal vapor jet is formed which originates from the molten pool surface and expands into the ambient gas (typically argon). The metal vapor jet then induces an argon gas flow that entrains the surrounding powders towards the jet, and once near the jet, the powders are immediately ejected following the expanding vapor flow. Despite such qualitative understanding of the powder-gas interaction in LPBF, the transient flow surrounding the powders as well as the gas-flow-induced forces on the powder surface have not been well quantified. Such quantitative information can be crucial to construct mappings between the powder motion to process parameters and to achieve the control of the powder motions.

---

<sup>1</sup> Contact author: wenda.tan@mech.utah.edu

Given that experimentally measuring the flow velocities and forces at such small scale ( $\sim 10$ s micron) can be very difficult to achieve, the multiphysics simulation is a ready tool for obtaining this quantitative information. In literature, the multiphysics simulations have been used to study the evolution of the molten pool and quantify physical phenomena such as key-holing [9], pore formation [10], lack-of-fusion [11] and balling [12]. For the gas flow, only the steady-state flow field have been simulated [1, 13], and up to the author's knowledge, no simulation work on the powder-gas interaction in LPBF can be found in literature. This lack of simulation effort can be attributed to the complexity of physics in the powder-gas interaction. Indeed, three phases, solid (metal powder), liquid (molten pool), and gas (metal vapor and argon), have to be modelled simultaneously and consistently to fully resolve the powder-gas interaction in LPBF.

In this work, a numerical model is developed to investigate the powder-gas interaction in LPBF. To cope with the complexity of physics, an incremental approach is taken such that only the solid and gaseous phase are resolved in the current model, while the liquid phase is neglected. The current model will provide the foundation for a more comprehensive model where all three phases are incorporated. The simulation results demonstrate the capability of the current model to capture the general trends of powder motions in LPBF, and to quantify the transient gas flow field and the forces of on the powders.

## 2. MODEL DESCRIPTION

A two-dimensional (2D) model is developed to capture the gas dynamics and the gas-flow-induced powder motions in a LPBF process. A computational fluid dynamics (CFD) module is used to calculate the pressure, velocity and temperature field in the gaseous phase. A particle-tracking (PT) module is used to calculate the forces, velocities and positions of powders. The CFD and PT module need to be coordinated to ensure consistent computations.

### Computational Fluid Dynamics Module:

In the gaseous phase, the conservation equations of mass, momentum, and energy for compressible flow constitute the governing equations to be solved, as written in Equations 1 – 3.

$$\frac{\partial \rho}{\partial t} + \nabla \cdot (\rho \vec{V}) = 0 \quad (1)$$

$$\frac{\partial}{\partial t}(\rho \vec{V}) + \nabla \cdot (\rho \vec{V} \vec{V}) = -\nabla p + \nabla \cdot \boldsymbol{\tau} \quad (2)$$

$$\begin{aligned} \frac{\partial}{\partial t}(\rho e) + \nabla \cdot (\rho e \vec{V}) &= \nabla \cdot (p \vec{V}) + \nabla \cdot (\boldsymbol{\tau} \vec{V}) \\ &+ \nabla \cdot (k \nabla T) \end{aligned} \quad (3)$$

In Equations 1 – 3,  $\rho$  is the density,  $\vec{V}$  is the velocity,  $p$  is the pressure,  $\boldsymbol{\tau}$  is the viscous tensor,  $\vec{g}$  is the gravitational acceleration,  $e$  is the total energy (internal energy and kinetic energy),  $k$  is the thermal conductivity, and  $T$  is the temperature. An in-house finite-volume CFD solver [14] is used to discretized and solve the governing equations for the gaseous phase.

### Particle-Tracking Module:

The Newton's equations of motion are solved to track the velocities of each individual powder, as written in Equations 4 and 5.

$$m_p \frac{d\vec{V}_{pc}}{dt} = \oint_{\partial S} \vec{F}_f dS + m_p \vec{g} + \vec{F}_{col} \quad (4)$$

$$I_p \frac{d\vec{\omega}}{dt} = \oint_{\partial S} \vec{r} \times \vec{F}_f dS \quad (5)$$

Equation 4 solves the translational velocity of powders where  $m_p$  is the powder mass and  $\vec{V}_{pc}$  is the velocity of the powder center. On the right-hand-side (RHS), the first term is the integration of the fluid-induced force ( $\vec{F}_f$ ) on the powder surface ( $\partial S$ ), the second term is the gravitational force, and the third term is the force due to powder-powder or powder-wall collisions. Here, the collision force  $\vec{F}_{col}$  is simplified to be a short-range repulsion force [15]. Equation 5 solves the rotational velocity of powders where  $I_p$  is the moment of inertia of powder and  $\vec{\omega}$  is the angular velocity of powder. The RHS is the integration of the fluid-induced torque on the powder surface. The positions of each powder, including the positions of powder center ( $x_{pc}$ ,  $y_{pc}$ ) and the angular position  $\theta$ , are updated according to the powder velocities ( $\vec{V}_{pc}$ ,  $\vec{\omega}$ ) by the Gear's time integration scheme.

### Coordination of Modules:

The coordination between the CFD and PT module is demonstrated in Figure 1. The CFD module calculation is carried out on a Cartesian grid where powders (e.g., the red circle) tracked by the PT module are overlaid. The grid cells whose centroid lies within the powder is identified as solid cells (gray cells) while the cells whose centroid lies outside the powder are identified as the gas cells. The simulation advances in time as the CFD module updates the pressure and velocity in each gas cells, and the PT module updates the velocities ( $\vec{V}_{pc}$ ,  $\vec{\omega}$ ) for each powder. For the solid cells, the pressure is extrapolated from the gas cells, and the velocity is assigned to be the local velocity of the powder.

To evaluate the fluid-induced force ( $\vec{F}_f$ ) in Equations 4 and 5, the Lagrangian points [16] are defined on the surface of each powder (purple points in Figure 1) and are fixed relative to the powder frame. The pressure and viscous stress are evaluated at each cell centroid of the Cartesian grid from CFD calculations, and are used to interpolate the fluid-induced forces ( $\vec{F}_f$ ) for each Lagrangian point. The surface integrals in Equations 4 and 5 are then obtained by integrating the force and torque over all Lagrangian points on the powder surface.

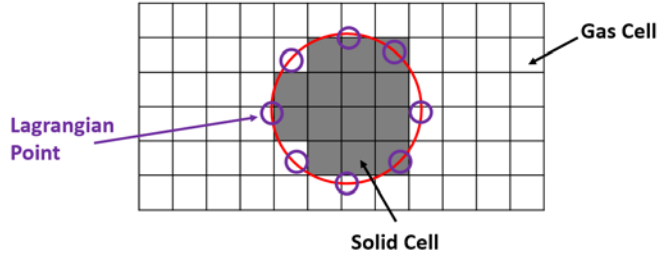


**Figure 1.** Coordination between the CFD and the PT module.

For each discrete time step of the simulation, the pressure and velocity in each Cartesian cell (both solid and gas) as well as the velocities and positions of each powder are determined. These quantities are then updated for the next time step with the procedure summarized as the following steps:

- 1) Interpolate the fluid-induced forces on Lagrangian points.
- 2) Evaluate the RHS of Equations 4 – 5, and update powder velocities and positions with the PT module.
- 3) Based on the updated powder positions, identify solid and gas cells.
- 4) Assign the pressure and velocity in solid cells, with the pressure in gas cells and the updated powder velocities.
- 5) Update the pressure and velocity in gas cells by solving Equations 1 – 3 with the CFD module.

### 3. PROBLEM DEFINITION

To cope with the complexity of physics in a real LPBF process, a simplified problem is formulated which resembles the process of LPBF but with simplified physics. The configuration of the problem is shown in Figure 2. The liquid phase (molten metal) is neglected and an artificial nozzle is defined to stimulate a free jet that resembles the metal vapor jet in a real LPBF process. The nozzle has a diameter  $D_N$  and a uniform inlet velocity of  $V_i$ . A set of powder particles is initially positioned at an offset distance  $d_o$  from the nozzle and is placed on a solid floor. The powder particles have a uniform diameter of  $d_p$  and are regularly positioned such as p1 – p5 shown in Figure 2. Significant change of temperature (e.g., powder melting and evaporation) is not considered in this problem and the inlet temperature of the nozzle is kept at room temperature. It is believed that by studying such a powder-jet interaction problem (Figure 2), the mechanisms of powder-gas interaction in a real LPBF process can be revealed.

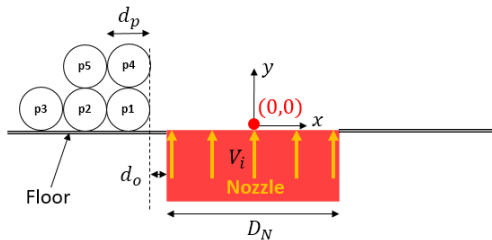


**Figure 2:** Configuration of the simplified problem (powder-jet interaction problem). The red circle indicates the origin of the coordinate system.

### 4. RESULTS AND DISCUSSION

The parameters of the powder-jet interaction, ( $D_N$ ,  $V_i$ ,  $d_o$ ,  $d_p$ ), are defined such that the configuration can resemble a typical LPBF process. Based on the typical experimental observations [2, 5], the following values are chosen:  $D_N = 200 \mu m$ ,  $V_i = 500 m/s$ ,  $d_o = 10 \mu m$ , and  $d_p = 50 \mu m$ . The powder material is chosen to be Ti-6Al-4V and the gas material is chosen to be argon. The material properties are assumed as temperature independent as the temperature variation in the simulations is not significant. The material properties at room temperature is taken, as listed in Table 1.

**Table 1.** Material properties of Ti-6Al-4V and argon gas used for simulation.

Material property	Ti-6Al-4V [17]	Argon [18]	Unit
Density	4420	1.78	kg m <sup>-3</sup>
Viscosity		$2.16 \times 10^{-5}$	Pa s

A series of case studies (listed in Table 2) are designed to investigate the formulated problem. In order to anatomize the details of powder-jet interaction, the cases are studied in which only a single powder particle is positioned beside the nozzle. Three different initial positions of the powder particle are investigated (Case 1 – 3), which correspond to the locations of p1, p2, and p3 in Figure 2. After the single-particle cases, a more realistic case is investigated in which four powder particles (corresponding to locations of p1, p2, p4 and p5 in Figure 2) are initially positioned besides the jet. In all the simulations, the Cartesian mesh size is  $5 \mu m$ , the time step size of  $0.01 \mu s$ , and a total time of  $500 \mu s$  is simulated.

**Table 2.** Powder-jet interaction study.

	Case No.	Corresponding particle(s) in Figure 2	Initial coordinates of particle center ( $\mu m$ )
Single particle	1	p1	(-135, 25)
	2	p2	(-185, 25)
	3	p3	(-215, 25)
Multiple particles	4	p1, p2, p4, p5	(-135, 25); (-185, 25); (-135, 75); (-185, 75)

#### 4.1 Interaction between Jet and One Single Particle

The simulation result for Case 2 is first discussed as a typical case for the single-particle studies. The simulated gauge pressure (difference between absolute pressure and 1 atm) and velocity field at 4 key time frames are shown in Figure 3a – 3d. The displacements ( $d_x$ ,  $d_y$ ), velocities ( $V_x$ ,  $V_y$ ), the subjected forces ( $F_x$ ,  $F_y$ ), angular position  $\theta$ , angular velocity  $\omega$ , and the subjected

torque  $\tau$  of the powder particle with respect to time are recorded and shown in Figure 4a – 4f.

Right after the simulation starts, the jet initiates from the nozzle and rapidly expands into the ambient gas. It is shown in Figure 3a that, at 2.5  $\mu\text{s}$ , the jet expansion creates a large vortex

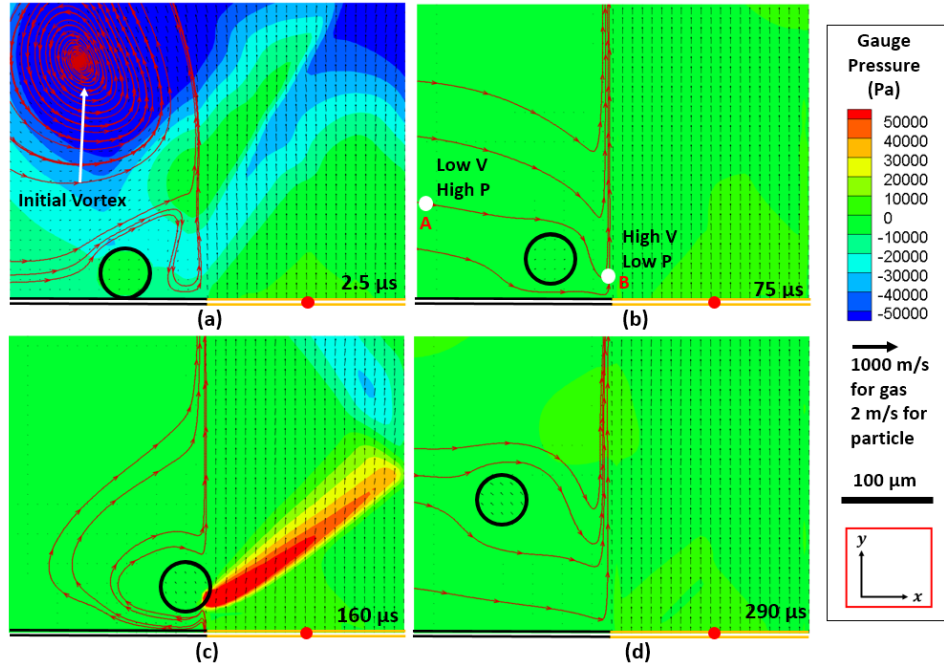


**Figure 3.** The pressure and velocity field at 2.5  $\mu\text{s}$ , 75  $\mu\text{s}$ , 160  $\mu\text{s}$  and 290  $\mu\text{s}$  of the simulation for the powder-jet interaction of a single powder particle (Case 2 in Table 2). The colored contours show the gauge pressure and the black arrows show the velocity field. The length of the arrow key represents 1000 m/s if the velocity arrow is in the gas and 2 m/s if in the velocity arrow is in the particle. The double black line stands for the floor and the double orange line stands for the nozzle. The red circle indicates the origin of the coordinate system. The red solid lines with arrows show the streamlines surrounding the powder particle.

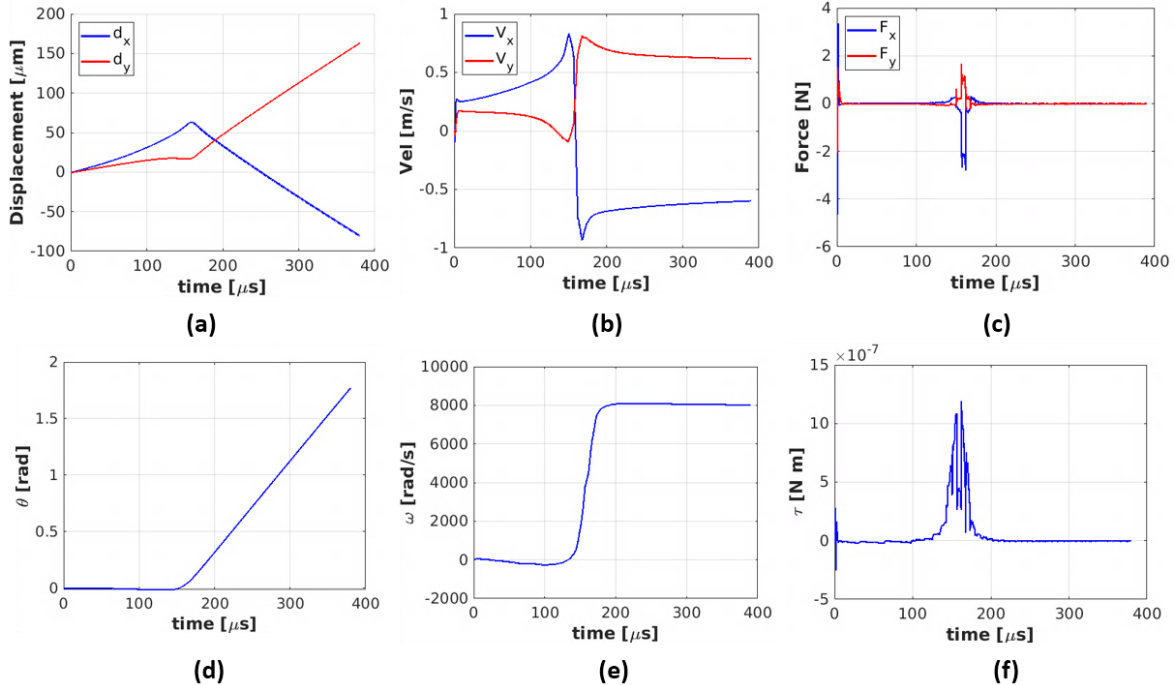


**Figure 4.** The displacements (a), velocities (b), the subjected forces (c), angular position  $\theta$  (d), angular velocity  $\omega$  (e), and the subjected torque  $\tau$  (f) of the powder particle with respect time for the single-particle simulation (Case 2 in Table 2).

that drives the powder particle upwards and towards the jet as indicated by the red streamlines surrounding the particle. This initial vortex rapidly propagates upwards and away from the particle with the free expansion of the jet at a velocity  $\sim 500$  m/s, and it only has significant influence on the powder motion for a very short period of time. It is observed in Figure 4c that the initial vortex leads to an “impulse” of the powder forces at the beginning of the simulation, which corresponds to a sharp increase of the powder velocities in Figure 4b ( $V_x$  increases to  $\sim 0.25$  m/s and  $V_y$  increases to  $\sim 0.2$  m/s). Thereafter, the powder forces are reduced to small values as the initial vortex propagates away from the powder.

During the time period of  $\sim 10 \mu\text{s} - 150 \mu\text{s}$ , the powder particle gradually accelerates along the +X direction and decelerates along the +Y direction as shown in Figure 4b. The “entrainment” of the particle towards the jet (along +X direction) has an acceleration  $\sim 3500 \text{ m/s}^2$  and a typical velocity  $\sim 0.5$  m/s. The entrainment motion can be explained by examining the streamlines at a typical time frame ( $75 \mu\text{s}$ ) during this time period as shown in Figure 3b. Two points, A and B, along a typical streamline are highlighted for the analysis. Point A is away from the jet and has a small velocity ( $\sim 5$  m/s) along the streamline. According to the Bernoulli principle, point A is associated with a larger gauge pressure ( $\sim -300$  Pa). Point B is located near the inlet of the jet and has large streamline-wise velocity ( $\sim 50$  m/s). Accordingly, point B has a lower gauge pressure ( $\sim -2000$  Pa) compared to point A. Due to the pressure difference between point A and B, the entrained gas bends towards the corner of the free jet (point B) and is then directed upwards along the expansion of the jet. Following this flow pattern, the particle is entrained and accelerates towards the corner of the jet.

As the powder particle continues to be entrained towards the jet, it eventually touches upon the jet around  $160 \mu\text{s}$  as shown in Figure 3c. A significant change of streamline pattern is resulted as the lower-right corner of the particle blocks the jet flow. The streamline-wise velocity reduces from  $\sim 500$  m/s at the inlet to almost zero at the particle surface. As a result, a focused high pressure region ( $\sim 40000$  Pa) is formed at the lower-right corner of the particle. This high pressure then “kicks” the particle along -X and +Y direction, as indicated by the “impulse” of powder forces in Figure 3c ( $F_x \sim -2$  N and  $F_y \sim 2$  N) and the sharp change of the powder velocities in Figure 3b ( $V_x$  changes from  $\sim 0.8$  m/s to  $\sim -0.9$  m/s and  $V_y$  changes from  $\sim -0.1$  m/s to  $\sim 0.8$  m/s); the acceleration of this dramatic transition is  $\sim 80000 \text{ m/s}^2$ . Also, there is an impulse of the torque around  $160 \mu\text{s}$  (Figure 3f) and accordingly, the angular velocity of the powder sharply increases to  $\sim 8000 \text{ rad/s}$  (Figure 3e). This torque is attributed to the tangential viscous forces on the powder surface which is created by the velocity difference between the vapor and the powder particle on the right side of the particle surface.

Resulted from the “kick”, the powder particle is ejected away from the jet and continues to move along the -X and +Y direction at a typical velocity  $\sim 1$  m/s (Figure 4b). It is noted that

the ejection of particle is against the surrounding flow, as the latter tends to entrain the particle towards the jet (the red streamlines in Figure 3d). Finally, the particle will be out of the calculation domain  $\sim 390 \mu\text{s}$  after which the particle is not tracked anymore in all the subfigures in Figure 4.

Consistent results can be obtained when the initial position of the powder particle is varied. Figure 5 shows the  $V_x$  and  $\omega$  with respect to time for Case 1 – 3 (Table 2). It is observed that all three simulations produce similar trend for the evolution of  $V_x$  and  $\omega$ . It is noted that for p1, the powder particle has a relatively short time period for the entrainment before it is ejected away from the jet, which is due to the proximity of the particle to the jet initially.

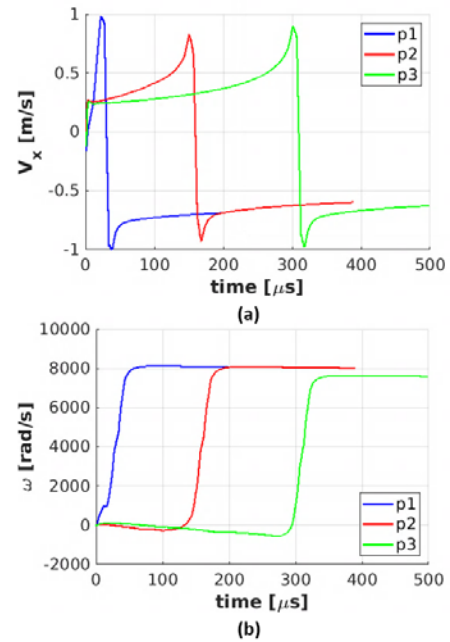


**Figure 5.** The X-velocity (a) and angular velocity (b) with respect to time for the powder-jet interaction of a single powder with different initial positions (Case 1 – 3 in Table 2). For each simulation, the powder is tracked until it has moved out of the calculation domain.

The single-particle simulations have revealed the powder-jet interaction in which the powder is driven by the surrounding gas flow to have the entrainment and ejection motions, while the gas flow can also be altered significantly by the powder blocking the jet. The simulated entrainment and ejection motions are analogous to those observed in LPBF processes. As a general comparison, the magnitude of powder entrainment and ejection velocity observed in LPBF processes are around 1 m/s and 5 m/s [2, 4, 5], while those from the current simulations are about 0.5 m/s and 1 m/s. The powder motions predicted by the current model can reasonably match the trends observed in experiments. Moreover, the simulations provides insightful information regarding the powder-jet interaction, such as pressure and velocity field, forces and torque on the powder, etc., which are difficult to measure by experiments.



## 4.2 Interaction between Jet and Multiple Particles

The interaction between the jet and four powder particles are investigated as a more realistic case in which the powder collisions as well as the powder-jet interaction are considered (Case 4 in Table 2). A time sequence of the simulated gauge pressure and velocity field is given in Figure 6a – 6f. Particle 1 is the first powder particle to be entrained and come in contact with the jet (Figure 6a), as it is the closest particle to the low pressure region at the left corner of the jet (point B in Figure 4b). Thereafter, particle 1 is ejected from the jet and sequentially collides with particle 2 and 3 (Figure 6b and 6c). Resulted from the collisions, particle 1 has a significant reduction in its momentum (both in the X and Y direction), particle 3 is directed towards the jet and is subsequently ejected (Figure 6c and 6d), and particle 2 gains a negative X velocity and moves away from the jet (Figure 6d). Then, particle 1 is slowly entrained towards the jet (Figure 6e) until it comes in contact with the jet for the second time and is subsequently ejected (Figure 6f). It is noted that at the last time frame of the sequence (Figure 6f), particle 2 and 3 have moved out of the calculation domain. This result demonstrates that, despite the simplified collision model, the general trend of powder collisions can be captured for the powder-jet interaction under investigation.

## 5. SUMMARY AND FUTURE WORK

In this work, a numerical model is established to investigate the powder-gas interaction in LPBF processes. The powder-gas interaction in a real LPBF process is simplified where the powder melting and metal vaporization is neglected, and an artificial free jet is used to model the metal vapor jet. In the study of the powder-jet interaction, the simulation results have shown the trend of powders being entrained towards and subsequently

ejected from the jet. It is also found that powders can cut into the jet to significantly alter its surrounding flow field. The simulated powder velocity for the entrainment ( $\sim 0.5$  m/s) and ejection ( $\sim 1$  m/s) motion can reasonably match with experimentally observed entrainment ( $\sim 1$  m/s) and ejection ( $\sim 5$  m/s) velocity in literature. The simulations provide insights into the driving forces for the powder motions by quantifying the pressure and velocity field, etc., which are difficult to measure by experiments. The driving forces can be attributed to the pressure differences in the gas flow surrounding the powder, as summarized below:

- When the powder is away from the jet, the gas velocity is increased from near the powder ( $\sim 5$  m/s) to the region near the jet ( $\sim 50$  m/s). By the Bernoulli principle, the pressure is decreased from the near the powder towards the jet with a pressure difference  $\sim 2000$  Pa, which gradually entrains the powder towards the jet at an acceleration of  $\sim 3500$  m/s<sup>2</sup> and a typical velocity of  $\sim 0.5$  m/s.
- When the powder comes into contact with the jet, the gas velocity dramatically decreases from the jet inlet ( $\sim 500$  m/s) to almost zero near the powder surface in contact with the jet. Therefore, a high pressure region ( $\sim 40000$  Pa) is formed where the powder cuts the jet and abruptly ejects the powder away from the jet at an acceleration of  $\sim 80000$  m/s<sup>2</sup> and a typical velocity of  $\sim 1$  m/s.

The current work provides the foundation for a series of future works, which are listed as follows:

- To incorporate the physics of laser heating of the powders.
- To incorporate the physics of powder melting and the vaporization.
- To investigate the interaction between the powders and the metal vapor jet.

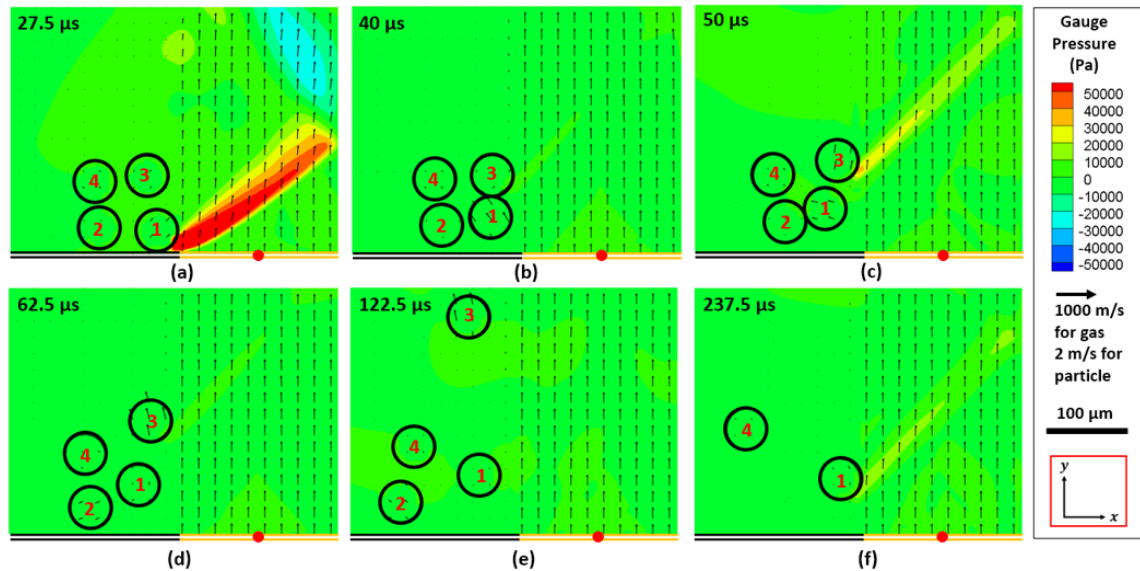


**Figure 6.** The time sequence of the simulated pressure and velocity field for the powder-jet interaction with multiple powders (Case 4 in Table 2). The colored contours show the gauge pressure and the black arrows show the velocity field. The double black line stands for the floor and the double orange line stands for the nozzle. The red circle indicates the origin of the coordinate system.

## ACKNOWLEDGEMENTS

The authors wish to gratefully acknowledge the financial support provided by the National Science Foundation under Grant No. CMMI-1933368 and the technical support from the Center for High-Performance Computing at the University of Utah.

## REFERENCES

- [1] Bidare, P., Bitharas, I., Ward, R., Attallah, M., and Moore, A., 2018, "Fluid and particle dynamics in laser powder bed fusion," *Acta Materialia*, 142, pp. 107-120.
- [2] Ly, S., Rubenchik, A. M., Khairallah, S. A., Guss, G., and Matthews, M. J., 2017, "Metal vapor micro-jet controls material redistribution in laser powder bed fusion additive manufacturing," *Scientific reports*, 7(1), p. 4085.
- [3] Matthews, M. J., Guss, G., Khairallah, S. A., Rubenchik, A. M., Depond, P. J., and King, W. E., 2016, "Denudation of metal powder layers in laser powder bed fusion processes," *Acta Materialia*, 114, pp. 33-42.
- [4] Guo, Q., Zhao, C., Escano, L. I., Young, Z., Xiong, L., Fezzaa, K., Everhart, W., Brown, B., Sun, T., and Chen, L., 2018, "Transient dynamics of powder spattering in laser powder bed fusion additive manufacturing process revealed by in-situ high-speed high-energy x-ray imaging," *Acta Materialia*, 151, pp. 169-180.
- [5] Zhao, C., Fezzaa, K., Cunningham, R. W., Wen, H., De Carlo, F., Chen, L., Rollett, A. D., and Sun, T., 2017, "Real-time monitoring of laser powder bed fusion process using high-speed X-ray imaging and diffraction," *Scientific reports*, 7(1), p. 3602.
- [6] Cunningham, R., Zhao, C., Parab, N., Kantzos, C., Pauza, J., Fezzaa, K., Sun, T., and Rollett, A. D., 2019, "Keyhole threshold and morphology in laser melting revealed by ultrahigh-speed x-ray imaging," *Science*, 363(6429), pp. 849-852.
- [7] Gong, H., Rafi, K., Gu, H., Starr, T., and Stucker, B., 2014, "Analysis of defect generation in Ti-6Al-4V parts made using powder bed fusion additive manufacturing processes," *Additive Manufacturing*, 1, pp. 87-98.
- [8] Nassar, A. R., Gundermann, M. A., Reutzel, E. W., Guerrier, P., Krane, M. H., and Weldon, M. J., 2019, "Formation processes for large ejecta and interactions with melt pool formation in powder bed fusion additive manufacturing," *Scientific reports*, 9(1), p. 5038.
- [9] Khairallah, S. A., Anderson, A. T., Rubenchik, A., and King, W. E., 2016, "Laser powder-bed fusion additive manufacturing: Physics of complex melt flow and formation mechanisms of pores, spatter, and denudation zones," *Acta Materialia*, 108, pp. 36-45.
- [10] Panwisawas, C., Qiu, C., Anderson, M. J., Sovani, Y., Turner, R. P., Attallah, M. M., Brooks, J. W., and Basoalto, H. C., 2017, "Mesoscale modelling of selective laser melting: Thermal fluid dynamics and microstructural evolution," *Computational Materials Science*, 126, pp. 479-490.
- [11] Bauereiß, A., Scharowsky, T., and Körner, C., 2014, "Defect generation and propagation mechanism during additive manufacturing by selective beam melting," *Journal of Materials Processing Technology*, 214(11), pp. 2522-2528.
- [12] Yan, W., Ge, W., Qian, Y., Lin, S., Zhou, B., Liu, W. K., Lin, F., and Wagner, G. J., 2017, "Multi-physics modeling of single/multiple-track defect mechanisms in electron beam selective melting," *Acta Materialia*, 134, pp. 324-333.
- [13] Masmoudi, A., Bolot, R., and Coddet, C., 2015, "Investigation of the laser-powder-atmosphere interaction zone during the selective laser melting process," *Journal of Materials Processing Technology*, 225, pp. 122-132.
- [14] Li, D., and Merkle, C. L., 2006, "A unified framework for incompressible and compressible fluid flows," *Journal of Hydrodynamics, Ser. B*, 18(3), pp. 113-119.
- [15] Glowinski, R., Pan, T.-W., Hesla, T. I., Joseph, D. D., and Periaux, J., 2001, "A fictitious domain approach to the direct numerical simulation of incompressible viscous flow past moving rigid bodies: application to particulate flow," *Journal of Computational Physics*, 169(2), pp. 363-426.
- [16] Uhlmann, M., 2005, "An immersed boundary method with direct forcing for the simulation of particulate flows," *Journal of Computational Physics*, 209(2), pp. 448-476.
- [17] Metals, A. S. M. A. S., 2004, "Titanium Ti-6Al-4V (Grade 5), ASM material data sheet," Florida, USA: ASM Aerospace Specification Metals Inc.
- [18] Michels, A., Botzen, A., and Schuurman, W., 1954, "The viscosity of argon at pressures up to 2000 atmospheres," *Physica*, 20(7-12), pp. 1141-1148.